Journal of Magnetic Resonance **155,** 92–99 (2002)
doi:10.1006/jmre.2001.2493, available online at http://www.idealibrary.com on IDEAL®

Multidimensional Imaging Using Combined Stray Field and Pulsed Gradients

J. Godward, E. Ciampi, M. Cifelli, and P. J. McDonald[1]

Department of Physics, School of Physics and Chemistry, University of Surrey, Guildford, Surrey GU2 7XH, United Kingdom

Received September 7, 2001; revised November 26, 2001; published online February 8, 2002

The paper describes an advance in stray field imaging (STRAFI) whereby images of planar samples can be obtained in the stray field of a superconducting magnet without the need for sample rotation. This is achieved by using the static stray magnetic field gradient in combination with pulsed orthogonal gradients. Results of both two- and three-dimensional implementations of the experiment are presented and discussed. An extension to diffusion-weighted imaging is introduced. The technique is expected to prove particularly useful in experiments where high resolution is required in only one direction while lower resolution is acceptable in the orthogonal directions, such as in studies of the drying and curing of paints and varnishes. Arising from the work, a new method for accurately calibrating the radiofrequency pulse width in stray field is found.

Key Words: **stray field imaging; STRAFI; pulsed field gradients.**

INTRODUCTION

Magnetic resonance microscopy is proving to be an important characterization tool in materials science (*1*), most notably for studies of liquid transport in solids and porous media, for studies of liquid flow through pipes and vessels, and for studies of dynamic processes such as cooking and polymer cross-linking. In our own work, we have investigated single and binary mixtures of solvents ingressing polystyrene (*2*), creaming and drying of emulsions layers (*3, 4*), and the drying and cross-linking of latex dispersion coatings (*5*). It is these latter activities which primarily prompt the technical developments reported here. To adequately study coatings systems we require a high spatial resolution of the order of 10 μm across a coating layer typically 100–300 μm thick with more moderate in-plane resolution to accommodate sample wrinkling and edge effects.

In MRI studies of many cross-linking dispersion coatings, there are two principal difficulties. The first is that the sample is initially wet and flows easily. In consequence it is not possible to readily move the sample, especially if it is being maintained in a controlled atmosphere. The second is that as the sample dries so the spin–spin relaxation time of the continuous and, more especially, the dispersed phase dramatically decreases leading to broad resonance lines. The former decreases due to increased liquid confinement, the latter due to increased cross-linking.

In recent years, many MRI methodologies have been developed to overcome the difficulties associated with the severe line broadening in solids (*6, 7*), including line-narrowing techniques (*8*), the use of fast oscillating gradients (*9*), and strong field gradients (*10*). Stray field imaging (STRAFI) (*11*) is a high gradient imaging method which offers high spatial resolution for systems with broad and moderately broad NMR linewidths (*12, 13*). The method exploits the large and extremely stable magnetic field gradient surrounding a standard high field magnet. In this gradient, a radiofrequency pulse excites nuclei in only a very thin slice of the sample orthogonal to the gradient. In a typical ^{1}H implementation, the gradient is of the order of 60 T/m and a pulse of 10 μs duration excites a slice approximately 40 μm thick. A one-dimensional profile is obtained by stepping the sample through the position of the resonant slice and acquiring NMR echo intensity data at each position. No Fourier transform is necessary. This can be done relatively quickly, as there is no need for spin–lattice relaxation delays between acquisition of successive slices. A well-averaged profile containing typically 128 data points can be acquired in a few tens of seconds. Two- and three-dimensional image data are conventionally obtained by additionally rotating the sample. However, this procedure is rarely carried out as the experiment becomes very time consuming. A particular advantage of STRAFI is that relaxation and diffusion contrast is readily retained in the NMR data through the use of spin echoes, albeit that a certain care has to be taken in interpreting echo train decay and modulation (*14–16*). Multidimensional demonstrations of STRAFI in the literature include early two-dimensional images of irregularly shaped polymer samples by Samoilenko *et al*. (*17*). Elsewhere, Zick (*18*) has obtained three-dimensional images of polycarbonate samples, and used T_2 contrast to assess solvent ingress. T_2 contrast was also employed in the three-dimensional work of Wang *et al*. (*19*) on "green" ceramics and the two-dimensional work of Iwamiya and Sinton (*20*) on various materials of interest to the aerospace industry.

The original STRAFI method, using a high field superconducting magnet, is still important, but lower cost alternatives dedicated to high field gradient work are now available. For

[1] To whom correspondence should be addressed. Fax: +44-(0)1483-686781. E-mail: p.mcdonald@surrey.ac.uk.

1090-7807/02 $35.00

instance, a permanent magnet with specially shaped pole pieces has been designed by the scalar potential method and built by Glover *et al*. (*21*). Dubbed GARField (gradient at right angles to field), the magnet offers a vertical field gradient orthogonal to the (horizontal) field direction that can be used to obtain one-dimensional profiles of planar samples weighted by all the usual relaxation-based NMR contrast parameters. For planar samples up to 500 μm thick, a short radiofrequency pulse can excite nuclei across the whole sample thickness and normal frequency encoding–Fourier inversion can be employed (*22, 23*). The field profile of GARField is highly tailored. In particular the magnitude of B_0 is constant in the horizontal plane although its direction varies slightly. We find that the improved geometry and field profile of GARField mean that for profiling coatings it outperforms (in terms of resolution, signal-to-noise, etc.) a high field STRAFI system. Another magnet geometry is the NMR-MOUSE developed by Blümich and Blümler and their respective co-workers (*24*). This uses the field produced by two anti-parallel polarized permanent magnets. In this case, however, the field profile, although known, is highly inhomogeneous. This poses severe practical problems for spatially localized work (*25*). A recent addition to the MOUSE involves an additional gradient coil pair and a Helmholtz pair type radiofrequency probe in the gap between the two magnets to obtain a one-dimensional profile (*26*). An alternative technique is the "planar imaging" experiment of Miller and Garroway (*27*), in which a large, planar sample is placed in a sensitive slice outside the body of the magnet. Information is acquired using a mechanically translated surface coil coupled with a swept frequency STRAFI sequence for depth resolution.

It is from these various developments, and of course conventional liquid-state MR microscopy methods (*22*), that we arrive at the method described in this paper. As already stated, and for the reasons given, it has been developed specifically for imaging planar coatings systems where both through-depth and transverse (lateral) liquid transport and polymer cross-linking play a role, but where sample rotation of the initially wet sample is impossible. To date high-resolution, one-dimensional profiling through the depth of coating systems has been achieved using GARField (*5*). Two-dimensional data have been obtained using conventional imaging techniques but has only been carried out for thicker layers (*3, 4*). The new method combines the advantages of the two: it provides the high-resolution characteristic of stray field methods through the depth of the layer, while resolving the in-plane directions at a lower resolution. Moreover it does this without the requirement of any sample movement or rotation. This is achieved by using the static stray field gradient in combination with switched, orthogonal gradients generated by appropriate current windings. This allows very high spatial resolution in the direction of the static gradient, together with more modest resolution in the orthogonal directions. The implementation described has been carried out using a high field superconducting system coupled with a commercial microscopy gradient set. This was purely for pragmatic reasons: the equipment was available. In time we envisage transferring the method to GARField and reaping the rewards of the much improved static field profile. However, this requires instrumentation development. The method is demonstrated both for ^{1}H density and for diffusion mapping in phantom samples.

RESULTS

(i) Sequence development. Figure 1a shows the basic pulse and gradient sequence proposed for two- and three-dimensional imaging in the stray field. The pulse sequence consists of two broadband radiofrequency pulses separated by τ which yield a narrow spin echo due to the large constant z gradient at time 2τ. The flip angle and relative phases of the pulses were varied as discussed below. However, in all cases the two pulse lengths were kept equal and the flip angles varied one to the other by varying the pulse amplitudes. The echo frequency encodes spatial information in the z direction across the resonant slice with an intensity modulation dependent on the pulse phases and flip angles. Only in the case of a sample sufficiently thin that the entire sample thickness is encompassed by the frequency bandwidth of the pulse can the excitation be considered uniform across the slice. Otherwise, the pulse selects a slice. Spatial information about the orthogonal (x, y) directions is phase encoded using switched x and y gradients applied in the first pulse interval. The equivalence of this sequence to well-known and established Fourier imaging sequences (*22*) is obvious—the unusual aspect is the use of the large static stray field gradient for both the frequency encode and the slice selection. Data processing consists of two- or three-dimensional Fourier transformation as appropriate.

One might prefer to use shaped radiofrequency pulses so as to excite a rectangular slice. However, the high gradient in the stray field means that soft, shaped pulses cannot excite a sufficiently

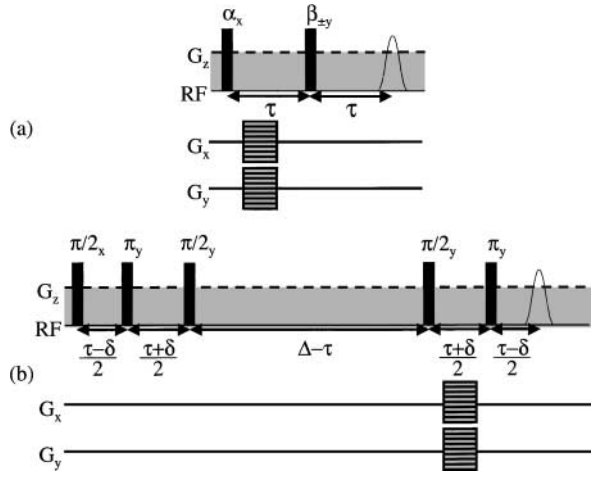

FIG. 1. Pulse and gradient sequence for (a) 3D FT STRAFI and (b) diffusion-weighted 3D FT STRAFI imaging with pulsed gradients. Spatial information about the x–y orthogonal directions is phase encoded using pulsed gradients.

thick slice for any practical application. Short shaped pulses have been proposed for regular STRAFI (*28*) but accurate shaping of extremely short pulses as required here is difficult. Hence we use hard pulses.

A number of authors have examined the spatial variation of magnetization and the modulation of echo amplitude for the pulse sequences commonly used in STRAFI. Benson and McDonald (*14*) considered the sequence α_x–τ–(α_y–τ–echo–τ–)$_n$, where $\alpha_{x/y}$ is a radiofrequency pulse of flip angle α and relative phase x or y and τ a short interval. They showed by numerical analysis and experiment that a maximum signal is obtained when α corresponds to approximately 120°. They also showed that the ratio of the first to second echo amplitudes is 2 to 3 when $\alpha = 90°$. The first echo is a direct Hahn echo while subsequent echoes contain contributions from direct and stimulated pathways at different locations across the slice. This sequence can produce very long trains of echoes which can be coadded to improve the signal-to-noise ratio of the data (*29*).

Later Bain and Randall (*15*) considered the sequence α_x–τ–(α_x–τ–echo–τ–)$_n$. This sequence does not produce the long echo trains preferred for STRAFI, as the direct and stimulated contributions to later echoes have varying phases that rapidly cancel each other and destroy the observed magnetization. However, it is found that the initial phase variation can be used to determine the pulse flip angle. A series of 90° pulses cause the first echo pair to be positive, the second negative, and so on. Most recently, Blümich and co-workers (*25*) and Hürlimann (*16*) have carried out extensive calculations of the combined effects of spin relaxation and diffusion on echo signals acquired using a variety of common sequences in inhomogeneous fields. Hürlimann in particular has realized a more general formalism for the necessary calculations.

In this work, we use only the first echo. Figure 2a shows results of numerical simulations. The Bloch equations have been integrated for the case of the α_x–τ–α_y–τ–echo sequence applied in the presence of a strong z gradient. The magnetization was evaluated as a function of space and time for the period $\tau/2$ to $3\tau/2$ following the second α pulse using the methodology described previously by Benson and McDonald (*14*). Simulated phase cycling ($\pm y$) of the second pulse was included so as to eliminate the unwanted free induction decay which this pulse generates. The magnetization was integrated over all space and Fourier transformed with respect to time to yield the magnetization profile for different values of α as shown in the figure. The simulation assumed ^{1}H NMR with parameters $\tau = 64$ μs, a pulse length of 10 μs, and a gradient strength of 28.7 T/m.

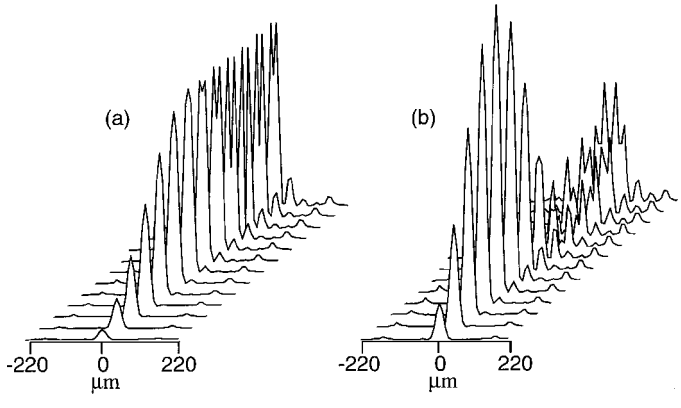

FIG. 2. Calculated magnetization slices as a function of pulse power obtained from the FT of the echo, for (a) α_x–τ–α_y–τ–echo and (b) α_x–τ–$2\alpha_y$–τ–echo pulse sequence, applied in the presence of a strong z gradient. The pulse length is 10 μs, τ is 64 μs, and the gradient is 28.7 T/m. Profiles are shown for flip angles α from 30° (bottom profile) to 210° (top profile) in steps of 15°. The vertical scaling is halved in (2b) relative to (2a).

The figure confirms how the maximum profile intensity occurs for a flip angle of the order of 120°. It also shows how, at higher flip angles, there is a substantial contribution to the signal arising from the lobes of the sinc function and how, by 180°, the intensity is zero at the center of the slice as expected. These results suggest an alternate means by which the 180° pulse length can be set in stray field imaging. One should seek the pulse flip angle for which the center of the Fourier-transformed echo recorded from a uniform sample is nulled. Figure 2b repeats the exercise for the sequence α_x–τ–$2\alpha_y$–τ–echo with similar parameters. This sequence is clearly preferred for Fourier STRAFI as the profile intensity is greater.

In addition to density mapping, applications to emulsion coatings demand the use of restricted pulsed field gradient diffusometry to characterize the coating droplet size and to observe any oil-in-water to water-in-oil phase inversion. To that end, we propose a modified form of a relaxation-compensated stimulated echo diffusion sequence for use in the stray field (*30, 31*). The basic sequence along with the modification, which consists of the spatial encoding gradients applied after the fourth radiofrequency pulse, is shown in Fig. 1b. In this sequence, the three 90° pulses constitute the well-known stimulated echo sequence routinely used for diffusion analysis. By keeping the intervals τ and Δ constant, attenuation by T_2 and T_1 relaxation is constant. The diffusive attenuation is partially refocused by the additional 180° pulse between the first two 90° pulses and again by the second 180° pulse ahead of the echo. The overall diffusion attenuation is determined by the balance of the compensated diffusion in the τ intervals and the uncompensated diffusion occurring during δ. The diffusion coefficient is therefore evaluated from measurements of the echo attenuation as a function of δ. A phase cycle is required to remove contributions from other coherence pathways giving rise to extra unwanted echoes. The overall echo amplitude, A, is given by (*30*)

$$A(\tau, \Delta, \delta, G) = \int e^{-\frac{1}{6}D(\gamma G)^2[\tau^3 - 3\tau^2\delta + 3(\tau + 2(\Delta-\tau))\delta^2 + 3\delta^3]} e^{-\frac{2\tau}{T_2}} e^{-\frac{(\Delta-\tau)}{T_1}}\, dz. \quad [1]$$

For the sequence to work well, one requires $6\Delta\delta^2 \geq \tau^3$, $T_2 \geq 2\tau$,

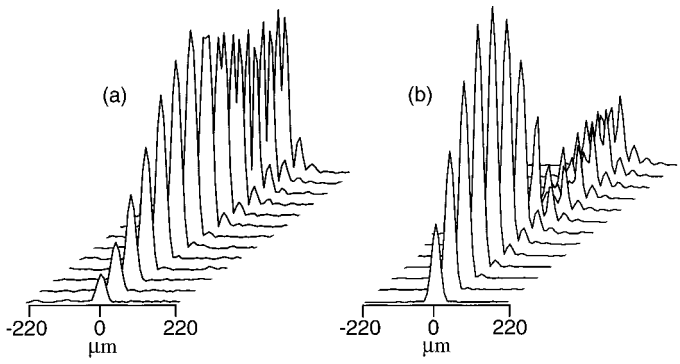

FIG. 3. Experimental magnetization slices of the central region of a cylindrical rubber phantom as a function of pulse amplitude, obtained from the FT of the echo, for (a) α_x–τ–α_y–τ–echo and (b) α_x–τ–$2\alpha_y$–τ–echo pulse sequence, applied in the presence of a strong z gradient. The pulse length is 10 μs, τ is 64 μs, and the gradient is 28.7 T/m. The pulse power is varied to obtain profiles directly comparable to the simulations shown in Figs. 2a and 2b, respectively. The vertical scaling is halved in (3b) relative to (3a).

and $T_1 \geq \Delta$ as well as a sufficiently fast diffusion coefficient. This requirement is not overly onerous.

In the modified sequence, the phase encoding gradients are used to spatially encode the in-plane magnetization of the excited slice. Fourier transformation with respect to the gradients yields transverse diffusion-weighted maps.

(ii) Sequence testing. Experimental verification of the results of the numerical simulation of the basic frequency encoding (profiling) sequence are presented in Figs. 3a and 3b. The figures show experimental profiles recorded from a central region of a cylindrical rubber bung much longer than the excited slice thickness. In producing Fig. 3a, the sequence used is α_x–τ–α_y–τ–echo and in Fig. 3b, α_x–τ–$2\alpha_y$–τ–echo. The profiles were obtained using a pulse length of 10 μs and a pulse gap, τ, of 64 μs. The pulse amplitudes are varied. The data can therefore be directly compared to Fig. 2. Good agreement is observed.

(iii) Density mapping. Initial imaging experiments were conducted on a sample of *blu-tac*. *Blu-tac* is a commercial soft polymer sold widely as an adhesive for fixing posters and paper notes to walls and other surfaces. The ^{1}H T_2 of *blu-tac* measured at 20 MHz using a CPMG sequence exhibits two components. The shorter is 3.3 ms (61%) and the longer 24.4 ms (39%). A small piece of the material was compressed into a PMMA mould 25 μm deep and 7.5 mm in diameter. Both two- and three-dimensional ^{1}H density maps were recorded. Figures 4a and 4b show central x–y and x–z image slices respectively extracted from one of the 3D data sets available, this one recorded with the α_x–τ–α_y–τ–echo sequence. These particular images were acquired using a pulse width of 2.2 μs, equivalent for the pulse amplitude used to a flip angle of 56°. The lower pulse length was chosen in order to increase the slice bandwidth so that it fully encompassed the sample. The pulse gap τ was 200 μs. This is typical of values which we use for many coatings systems. It is long enough to well resolve the *blu-tac* and to suppress the signal from the PMMA. We note that a component of the PMMA is sufficiently mobile to be weakly seen in images recorded with τ of just 80 μs. Echoes were recorded at a sampling rate of 800 kHz for an acquisition time of 80 μs. The z static field gradient is 28.7 T/m. The x and y phase encoding gradients were applied for 100 μs, and ranged between ±0.32 T/m in 32 steps; 256 averages were coadded and each 3D experiment took a total of about 18 h to perform. The calculated pixel sizes are thus 5.1 μm in the z direction and 370 μm in the x–y directions.

The x–z image (Fig. 4b) shows that the sample is only moderately well aligned orthogonal to the magnetic field. Accurate alignment is extremely difficult to achieve in the *bricollage* experimental probe. The image also shows the layer to be a little thicker than the expected 25 μm. It is, in fact, between 30 and 40 μm thick. This is due to the natural elasticity of *blu-tac* which tends to restore the flattened disc to the spheroid from which it was pressed.

The x–y slice (Fig. 4a) shows the phantom disc cutting the plane extracted from the data set. This is to be expected given the poor horizontal alignment of the sample relative to the field. A projection of the entire image data set onto the x–y plane reveals most of the full circle: it is slightly incomplete as the experimental bandwidth is falling off rapidly at the extremes (Fig. 4c). In order to alleviate this attenuation as much as possible, the projected planes have been weighted by the reciprocal

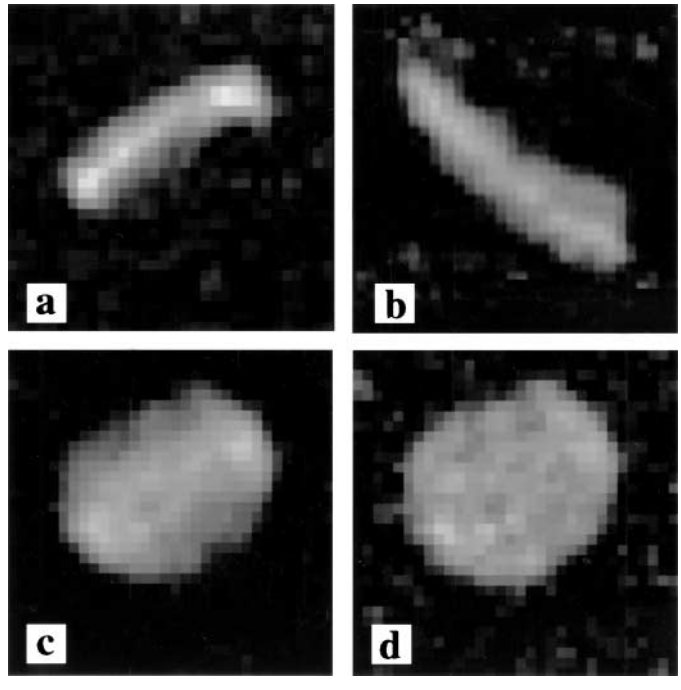

FIG. 4. 3D FT STRAFI imaging of a *blu-tac* phantom. (a) The central x–y slice extracted from the 3D data set. The field of view is 11.8 × 11.8 mm. (b) The central x–z slice. The region of interest shown is 11.8 × 0.176 mm. (c) Projection of the sum of 28 central x–y slices (±71 μm from the center). (d) Projection of the sum of the 28 central x–y slices weighted by the reciprocal of the theoretical z-profile magnetization intensity.

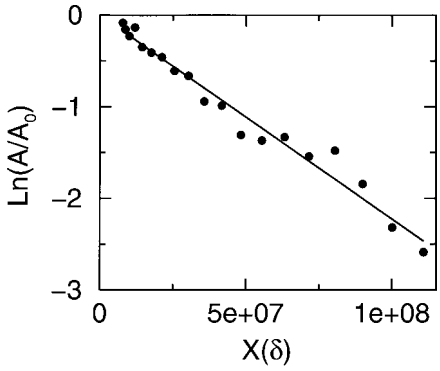

FIG. 5. Semilogarithmic plot of the echo attenuation A/A_0, where A_0 is the echo amplitude for $\delta = 0$ for a water sample at room temperature, measured with the sequence in Fig. 1b without phase encoding gradients. $X(\delta) = (\gamma G)^2(-3\tau^2\delta + 3(\tau + 2(\Delta - \tau))\delta^2 + 3\delta^3)$. The solid line represents the best fit to the data and yields $D = 2.24 \times 10^{-9}$ m^2 s^{-1}.

of the expected z-profile intensity arising from calculations such as those used to generate Fig. 2. This has been done in producing Fig. 4d, which is the sum of the weighted x–y image slices between ± 71 μm around the center. The limits have been set so as to include only those planes encompassed by the pulse bandwidth.

(iv) Diffusion mapping. Figure 5 shows the results of a simple measurement (not spatially resolved) from which the diffusion coefficient of bulk water was obtained using the sequence shown in Fig. 1b without phase encoding gradients. The calculated diffusion coefficient is 2.24×10^{-9} m^2 s^{-1} in excellent agreement with published values (*32*).

The diffusion-weighted imaging sequence was tested using an oil-in-heavy water emulsion. The emulsion consisted of decane (33.3 wt%) in a D_2O solution (66.6 wt%) containing 1.0 wt% Tween 80 surfactant. The emulsion was mixed using an Ultra Turrax T8 (IKA Labortechnik, Germany) homogenizer for 90 min. The emulsion droplet size distribution was measured using an optical microscope. Emulsion droplet sizes are generally well characterized by a lognormal distribution function. However, for reasons to become apparent, we prefer to fit to a Gaussian volume distribution function,

$$P_v(r) = \frac{A}{\sigma\sqrt{2\pi}} \exp\left(\frac{-(r - r_0)^2}{2\sigma^2}\right), \qquad [2]$$

where $r_0 = 2.0$ μm is the measured mean droplet radius and $\sigma = 0.5$ is the standard deviation. The emulsion is thus very similar to ones we have previously used and reported on elsewhere (*33*).

For the imaging experiment, the emulsion was allowed to cream and then four empty capillaries of internal diameter 0.9 mm and external diameter 1.7 mm were passed through the cream layer. Density maps, an example of which is shown in Fig. 6a, were collected across the cream and capillaries using the sequence of Fig. 1a with $\tau = 120$ μs and phase gradients between ± 0.96 T/m in 32 steps applied for 30 μs. The most obvious feature is the empty capillaries positioned around the edge of the cream layer. Subsequently, two of the capillaries

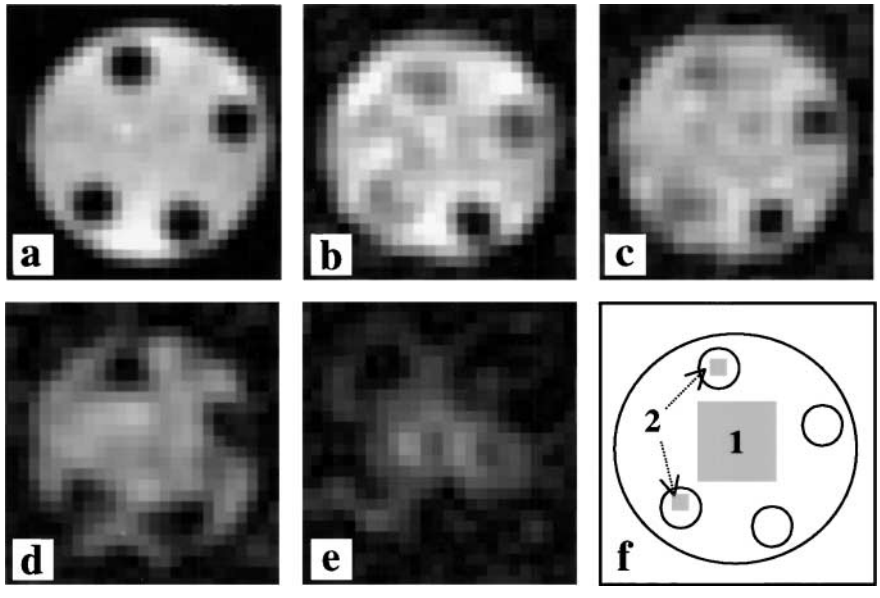

FIG. 6. (a) Region of interest (10 × 10 mm) of the central x–y slice of a 3D FT STRAFI ^{1}H density data set of a decane-in-heavy water emulsion cream containing four empty capillaries. The intensity is scaled by 0.4. (b) Region of interest of the central x–y slice extracted from a diffusion-weighted 3D FT STRAFI data set of the decane-in-heavy water emulsion cream containing two capillaries filled with pure decane and two empty capillaries, recorded with $\delta = 20$ μs and $\Delta = 2$ ms, (c) $\delta = 40$ μs and $\Delta = 2$ ms, (d) $\delta = 20$ μs and $\Delta = 128$ ms, and (e) $\delta = 40$ μs and $\Delta = 128$ ms. (f) Schematic identifying the regions used to calculate the average pixel intensity for the cream, 1, and for the pure decane in the filled capillaries, 2. All images are displayed using a common gray scale.

were filled with pure decane and diffusion-weighted maps were acquired with the sequence of Fig. 1b using $\tau = 200$ μs with $\delta = 20$ and 40 μs for each of $\Delta = 2$ and 128 ms. The phase encoding gradients were applied for 30 μs in 16 steps between ± 0.48 T/m and the data were zero-filled. The in-plane pixel size is therefore 410 μm, comparable to the capillary dimensions. Four central transverse slices are shown in Figs. 6b to 6e, respectively.

The diffusion-weighted image acquired with $\delta = 20$ μs and $\Delta = 2$ ms (Fig. 6b) is very similar in appearance to the density map except that two of the capillaries are now filled. The signal-to-noise ratio of the image data is considerably worse than that in Fig. 6a. This can be attributed to three causes. First, there is more diffusion attenuation in Fig. 6b. Second, the stimulated echo sequence only stores and encodes half of the magnetization. Third, Fig. 6a was recorded with the preferred α–τ–2α sequence.

Across the total diameter of the filled capillaries, taking account of the wall thickness, the filling factor is $(0.9/1.7)^2 = 0.28$. The filling factor for the droplets in the cream layer is in excess of 0.64, the value expected for close-packed spheres of equal size (*34*). Hence one expects the average image intensity in the cream to exceed that in the capillaries by a factor approaching 2.5. The average single pixel intensity for an extended and representative region of the cream (defined by region 1 in Fig. 6f) has been measured and found to be approximately 1.5 times that in the vicinity of the filled capillaries. Given the approximation used in locating the capillaries, this is a reasonable result.

The image data of Fig. 6b can be used in conjunction with that acquired with $\delta = 40$ μs and $\Delta = 2$ ms, Fig. 6c, to estimate the diffusion coefficient for the decane in the filled capillaries and for the decane in the cream. Using the same pixel averaging as before, we calculate the former to be 1.44×10^{-9} m^2 s^{-1} and the latter to be 1.49×10^{-9} m^2 s^{-1}. The two values are very similar, indicative of decane not experiencing restricted diffusion. For comparison, a typical literature value for the diffusion coefficient of decane is 1.38×10^{-9} m^2 s^{-1} (*35*).

The image data shown in Fig. 6d was acquired with $\delta = 20$ μs and $\Delta = 128$ ms. They reveal the effects of restricted diffusion in the cream. The intensity in the filled capillaries is very much less than in the cream. Indeed, in the capillaries, the image intensity is close to background and it is hard to make reliable quantitative measurements. In contrast the signal intensity in the cream remains about 0.67 that in the comparable image with $\Delta = 2$ ms.

The last image, Fig. 6e, was acquired with $\delta = 40$ μs and $\Delta = 128$ ms. The ratio of the signal intensity in the cream region of the two images acquired with $\Delta = 128$ ms is 0.46. Tanner and Stejskal (*36*) considered a standard pulsed field gradient stimulated echo sequence without the 180° refocusing pulses. They calculated the echo attenuation in the long time limit ($\Delta \to \infty$) arising from restricted diffusion in a field gradient for the case of spherical drops. Subsequently, Callaghan *et al.* (*37*) showed that their result could be approximated by a Gaussian function and analytically integrated over a Gaussian volume distribution of droplet sizes. The result is

$$A = A_0 \frac{1}{\sqrt{1 + 2\sigma^2 \beta^2}} \exp\left(- \frac{\beta^2 r_0^2}{1 + 2\sigma^2 \beta^2} \right), \qquad [3]$$

with $\beta^2 = \gamma^2 G^2 \delta^2 / 5$, r_0 the mean droplet radius, and σ the standard deviation. If the assumption is made that the sequence actually used (Fig. 1b) is comparable insomuch as it consists of two gradient pulses of duration δ separated by $(\Delta - \tau)$, then the expected ratio of the cream intensities based on the optical measurements of the droplet size distribution is 0.5. Given the approximations used in deriving Eq. [3] and the even greater approximations in applying it to the current circumstance this represents good agreement with the measured value of 0.46 and strongly suggests that we are observing the effects of restricted diffusion in the maps obtained in the stray field. We believe that this is the first time that any such spatially resolved stray field measurement has been made.

(v) Image distortion. One question to be addressed about imaging in the stray field concerns distortions due to the curvature of the stray field. There are two, related, problems. First, the z component of the magnetic field, B, at a given z coordinate beneath the magnet varies radially. Second, the direction of the magnetic field deviates away from the z direction at increasing radius, r. As a result, the excited slice is not planar, but rather concave or convex in shape and the direction about which the magnetization precesses varies. This causes distortion of the image primarily in the z (frequency-encoded) direction.

In order to assess the significance of these effects on the data shown, we have transformed the data according to our best estimates of the true field profile. The shift, δz, in the z direction is given by

$$\delta z(r', z') = \frac{B(0, z') - B(r', z')}{\frac{\partial B}{\partial z}\big|_{z', r'}}, \qquad [4]$$

where $B(r', z')$ is the field magnitude at location (r', z').

The pixel intensity, I, is correspondingly scaled according to

$$I = I_0 \left(1 + \frac{d(\delta z)}{dz} \right). \qquad [5]$$

The transformation assumes that the phase encoding gradients are linear and that the phase gradients do not significantly further distort the main field profile.

Field data plots were obtained from the manufacturers of the magnet and, in the area of the slice of interest, were fitted to the far field pattern of a magnetic dipole. This fitting was surprisingly good over the limited spatial range in question. This information was used to transform the image data shown in Fig. 4b. The result is shown in Fig. 7. The transformation has clearly improved the image. Initial curvature has been removed and the

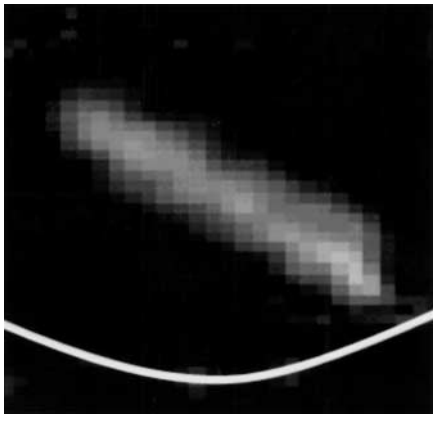

FIG. 7. The central x–z slice shown in Fig. 4b transformed using Eqs. [4] and [5]. The white line indicates the field curvature in the (not transformed) image plane.

image is nearer the expected "regular" shape. Correction for the pulse bandwidth comparable to that used in Fig. 4d has also been included. If anything, the transformation has overcorrected the curvature and reversed it. This is likely due to the limitations of the field profile data. Small, weakly magnetic parts around the magnet gently distort the field in an unspecified manner.

CONCLUSIONS

This paper has introduced three-dimensional STRAFI without sample movement, and presented an appropriate pulse sequence for this purpose. Pixel resolution in the z direction of the order of 5 μm is obtained. The resolution in the radial direction is much less, but still useful for "gently curving" planar samples.

The method should thus prove useful in measurements of, for instance, film formation from dispersions where high resolution is required through the film depth coupled with more modest resolution in plane. The technique will also be useful for studies of solvent ingress into polymer surfaces and layers, where swelling is rarely one-dimensional as commonly assumed. Although slow in comparison to the one-dimensional experiment, the method can be used at the end of a time course study to assess curvature.

The main difficulty associated with the method is the narrow excitation bandwidth. However, it should be possible to image a larger sample by sweeping the transmitter frequency, in much the same way as Mallett *et al*. (*38*). As before, slice interleaving will save relaxation delays and not unduly increase the total experimental time.

EXPERIMENTAL

Experiments were performed in the fringe field gradient of a 9.4-T Magnex (UK) superconducting magnet. The exact position corresponded to a ^{1}H resonance frequency of 99.85 MHz (equivalent to ^{13}C at magnet isocenter) and was located 302 mm below the isocenter. At this position, the nominal field gradient in the vertical (z) direction of the magnet is 2.870 T/m. The position and gradient were identified from a magnetic field plot supplied by Magnex. A Resonance Research (U.S.A.) 3D microimaging gradient set was lowered on lengths of brass studding so as to be centered at this position. A Resonance Research shim gradient set was held in its usual place in the magnet bore to support the gradients but performed no additional useful purpose. The NMR probe was a double-resonance 400/100 imaging probe supplied by Frauenhoefer Institute, Germany, containing a saddle coil. The probe is otherwise routinely used for ^{13}C/^{1}H cross-polarization experiments and has excellent RF homogeneity over the sample volume. NMR pulse sequences were run using a Chemagnetics Infinity-VME console (U.S.A.).

ACKNOWLEDGMENTS

J.G. thanks the UK Engineering and Physical Science Research Council for support. E.C. thanks Unilever Research for financial support. M.C. thanks the University of Pisa, Italy, for financial support.

REFERENCES

1. J. B. Miller, NMR imaging of materials, *Prog. Nucl. Magn. Reson. Spectrosc.* **33,** 273–308 (1998).
2. R. Sackin, E. Ciampi, J. Godward, J. L. Keddie, and P. J. McDonald, Fickian ingress of binary solvent mixtures into glassy polymer, *Macromolecules* **34,** 890–895 (2001).
3. E. Ciampi, U. Goerke, J. L. Keddie, and P. J. McDonald, Lateral transport of water during drying of alkyd emulsions, *Langmuir* **16,** 1057–1065 (2000).
4. J. M. Salamanca, E. Ciampi, D. A. Faux, P. M. Glover, P. J. McDonald, A. F. Routh, A. C. I. A. Peters, R. Satguru, and J. L. Keddie, Lateral drying in thick films of waterborne colloid particles, *Langmuir* **17,** 3202–3207 (2001).
5. M. Wallin, P. M. Glover, A. C. Hellgren, J. L. Keddie, and P. J. McDonald, Depth profiles of polymer mobility during the film formation of a latex dispersion undergoing photoinitiated cross-linking, *Macromolecules* **33,** 8443–8452 (2000).
6. B. Blümich, "NMR Imaging of Materials," Oxford Univ. Press, Oxford (2000).
7. P. Blümler and B. Blümich, NMR imaging of solids, *in* "NMR Basic Principles and Progress" (P. Diehl, E. Flock, and R. Konsfeld, Eds.), Springer-Verlag, Berlin (1994).
8. D. E. Demco and B. Blümich, Solid-state NMR imaging methods. Part II. Line narrowing, *Concepts Magn. Reson.* **12,** 269–288 (2000).
9. S. P. Cottrell, M. R. Halse, and J. H. Strange, NMR imaging of solids using large oscillating field gradients, *Meas. Sci. Technol.* **1,** 624–629 (1990).
10. D. E. Demco and B. Blümich, Solid-state NMR imaging methods. Part I. Strong field gradients, *Concepts Magn. Reson.* **12,** 188–206 (2000).
11. A. A. Samoilenko, D. Y. Artemov, and L. A. Sibeldina, Formation of sensitive layer in experiments on NMR subsurface imaging of solids, *JETP Lett.* **47,** 417–419 (1988).
12. P. J. McDonald, Stray field magnetic resonance imaging, *Prog. Nucl. Magn. Reson. Spectrosc.* **30,** 69–99 (1997).
13. P. J. McDonald and B. Newling, Stray field magnetic resonance imaging, *Rep. Prog. Phys.* **61,** 1441–1493 (1998).

14. T. B. Benson and P. J. McDonald, Profile amplitude modulation in stray-field magnetic-resonance imaging, *J. Magn. Reson. A* **112,** 17–23 (1995).

15. A. D. Bain and E. W. Randall, Hahn spin echoes in large static gradients following a series of 90° pulses, *J. Magn. Reson. A* **123,** 49–55 (1996).

16. M. D. Hürlimann, Diffusion and relaxation effects in general stray field NMR experiments, *J. Magn. Reson.* **148,** 367–378 (2001).

17. A. A. Samoilenko, D. Y. Artemov, and L. A. Sibeldina, *1987a Bruker Report* **2,** 30–31 (1987).

18. K. Zick, "STRAFI Solids Imaging," Technical Report NMR/B353/393, Bruker Anlytische Messtechnik GmbH Silberstreifen, D-7512 Rheinstetten 4/Karlsruhe (1993).

19. P. S. Wang, D. B. Minor, and S. G. Malghan, Binder distribution in SI3N4 ceramic green bodies studied by stray-field NMR imaging, *J. Mater. Sci.* **28**(18), 4940–4943 (1993).

20. J. H. Iwamiya and S. W. Sinton, Stray-field magnetic resonance imaging of solid materials, *Solid State Nucl. Magn. Reson.* **6,** 333–345 (1996).

21. P. M. Glover, P. S. Aptaker, J. R. Bowler, E. Ciampi, and P. J. McDonald, A novel high-gradient permanent magnet for the profiling of planar films and coatings, *J. Magn. Reson.* **139,** 90–97 (1999).

22. P. T. Callaghan, "Principles of Nuclear Magnetic Resonance Microscopy," Clarendon Press, Oxford (1991).

23. A. A. Samoilenko, Solid state imaging of X-nuclei distributions and layer structures by STRAFI method, *in* "28th Congress Ampere, Extended Abstracts" (M. E. Smith and J. H. Strange, Eds.), University of Kent at Canterbury Print Unit, Canterbury (1996).

24. B. Blümich, P. Blümler, G. Eidmann, A. Guthausen, R. Haken, U. Schmitz, K. Saito, and G. Zimmer, The NMR-MOUSE: Construction, excitation, and applications, *Magn. Reson. Imaging* **16,** 479–484 (1998).

25. F. Balibanu, K. Hailu, R. Eymael, D. E. Demco, and B. Blümich, Nuclear magnetic resonance in inhomogeneous magnetic fields, *J. Magn. Reson.* **145,** 246–258 (2000).

26. P. J. Prado, B. Blümich, and U. Schmitz, One-dimensional imaging with a palm-size probe, *J. Magn. Reson.* **144,** 200–206 (2000).

27. J. B. Miller and A. N. Garroway, Planar imaging by NMR, *in* "Proceedings, 35th Experimental Nuclear Magnetic Resonance Conference (April 10–15, 1994)," Pacific Grove, CA, p. 186.

28. A. A. Samoilenko, Personal communication.

29. E. W. Randall, A. A. Samoilmenko, and R. Q. Fu, Hahn-echo for N-14 solids by the stray field method: Prospects for imaging using long echo-trains summation, *Solid State Nucl. Magn. Reson.* **14,** 175–179 (1999).

30. R. Kimmich, Relaxation compensated pulse sequences, *in* "NMR: Tomography, Diffusometry, Relaxometry," pp.187–190, Springer-Verlag, Heidelberg (1997).

31. R. Kimmich and E. Fischer, One dimensional and two dimensional pulse sequences for diffusion experiments in the fringe field of superconducting magnets, *J. Magn. Reson. A* **106,** 229–235 (1994).

32. R. Mills, Self-diffusion in normal and heavy water in the range 1–45°, *J. Phys. Chem.* **77,** 685–688 (1973).

33. P. J. McDonald, E. Ciampi, J. L. Keddie, M. Heidenreich, and R. Kimmich, Magnetic-resonance determination of the spatial dependence of the droplet size ditribution in the cream layer of oil–water emulsion: Evidence for the effects of depletion flocculation, *Phys. Rev. E* **59,** 874–884 (1999).

34. E. Dickinson, *in* "Food Structure—Its Creation and Evaluation" (J. M. Blareshard and J. R. Mitchell, Eds.), pp. 48–54, Butterworths, London (1988).

35. I. Lönnqvist, B. Håkansson, B. Balinov, and O. Söderman, NMR self-diffusion of the water and the oil components in a W/O/W emulsion, *J. Colloid Interface Sci.* **192,** 66–73 (1997).

36. J. E. Tanner and E. O. Stejskal, Restricted self-diffusion of protons in colloidal systems by the pulsed-gradient, spin-echo method, *J. Chem Phys.* **49,** 1768–1777 (1968).

37. P. T. Callaghan, K. W. Jolley, and R. S. Humphrey, Diffusion of fat and water in cheese as studied by pulsed field gradient nuclear magnetic resonance, *J. Colloid Interface Sci.* **93,** 521–529 (1983).

38. M. J. D. Mallett, M. R. Halse, and J. H. Strange, Stray field imaging by magnetic field sweep, *J. Magn. Reson.* **132,** 172–175 (1998).